

SCIENTIFIC REPORTS

OPEN

On the small angle twist sub-grain boundaries in Ti_3AlC_2

Hui Zhang^{1,2}, Chao Zhang¹, Tao Hu^{1,2}, Xun Zhan³, Xiaohui Wang¹ & Yanchun Zhou⁴

Received: 13 October 2015

Accepted: 16 March 2016

Published: 01 April 2016

Tilt-dominated grain boundaries have been investigated in depth in the deformation of MAX phases. In stark contrast, another important type of grain boundaries, twist grain boundaries, have long been overlooked. Here, we report on the observation of small angle twist sub-grain boundaries in a typical MAX phase Ti_3AlC_2 compressed at 1200 °C, which comprise hexagonal screw dislocation networks formed by basal dislocation reactions. By first-principles investigations on atomic-scale deformation and general stacking fault energy landscapes, it is unequivocally demonstrated that the twist sub-grain boundaries are most likely located between Al and Ti4f (Ti located at the 4f Wyckoff sites of $P6_3/mmc$) layers, with breaking of the weakly bonded Al–Ti4f. The twist angle increases with the increase of deformation and is estimated to be around 0.5° for a deformation of 26%. This work may shed light on sub-grain boundaries of MAX phases, and provide fundamental information for future atomic-scale simulations.

Ti_3AlC_2 is an essentially important member in the family of machinable layered ternary carbides and nitrides^{1,2}, whose chemical formula can be generalized as $M_{n+1}AX_n$ (referred to as MAX phases; M is an early transition metal element; A is an A group element; X is C or N; n is an integer)^{1–7}. Combining the merits of ceramics and metals, MAX phases are of vital technological importance^{2,4–6}. Like ceramics, they exhibit high elastic stiffness and strength, good oxidation and corrosion resistance; like metals, they have high electrical and thermal conductivity, excellent machinability and thermal shock resistance^{1–7}.

In the deformation of MAX phases, dislocations play a crucial role. The dislocations in uniaxially deformed MAX phases are predominantly confined in the basal plane^{8–13}. Out-of-basal-plane dislocations have only been observed in nanoindented Ti_3SnC_2 ¹⁴, Ti_2AlN deformed at 900 °C under gaseous confining pressure¹⁵ and slowly compressed Ti_3AlC_2 at 1200 °C¹¹. Basal dislocations are prone to be arranged in arrays within the basal plane or walls along [0001]⁹. The accumulation of dislocation arrays within the basal plane gives rise to the bending of the basal plane, while that of dislocation walls leads to the formation of kinking boundaries.

Kinking boundaries in MAX phases are special tilt-dominated grain boundaries with limited twist components^{8,9}. Farber *et al.* interpreted the kinking boundaries as dislocation walls with perfect dislocations threading along [10 $\bar{1}$ 0]⁸, wherein the dislocations alternatively have a Burgers vector of $1/3[1\bar{1}\bar{2}0]$ and $1/3[\bar{2}110]$. An excess of one type of dislocation (e.g. $1/3[1\bar{1}\bar{2}0]$) over the other (e.g. $1/3[\bar{2}110]$) contributes to the twist components⁸. Twist grain boundaries, on the contrary, can be regarded as screw dislocation networks^{16,17}. For instance, small angle twist (sub-) grain boundaries (SATGBs) in the typical oxide ceramics Al_2O_3 , (0001)/[0001], consist of hexagonal screw dislocation networks (HSDNs) with $1/3\langle 1\bar{1}\bar{2}0 \rangle$ basal dislocations¹⁸. The SATGBs in face- (with high stacking fault energy) and body-centered cubic metals comprise HSDNs as well^{16,17,19,20}. In this letter, the dislocation segments of previously observed hexagonal networks in Ti_3AlC_2 ¹¹ are determined to be screw type, and further, the formation and evolution of HSDNs/SATGBs are closely investigated.

Results

Formation of HSDNs. Basal dislocations in MAX phases can react to form complex dislocation networks and dense hexagonal cells¹². In transmission electron microscopy (TEM) specimens sampled along directions both vertical and parallel to the load, hexagonal dislocation networks were frequently observed near the grain boundaries, wherein the dislocations are prone to be initiated or piled up. Figure 1a shows the typical TEM

¹Shenyang National Laboratory for Materials Science, Institute of Metal Research, Chinese Academy of Sciences, 72 Wenhua Road, Shenyang 110016, China. ²University of Chinese Academy of Sciences, Beijing 100049, China. ³Department of Materials Science and Engineering, Case Western Reserve University, 10900 Euclid Ave, Cleveland, OH, 44106, USA. ⁴Science and Technology on Advanced Functional Composite Laboratory, Aerospace Research Institute of Materials & Processing Technology, No. 1 South Dahongmen Road, Beijing 100076, China. Correspondence and requests for materials should be addressed to X.W. (email: wang@imr.ac.cn)

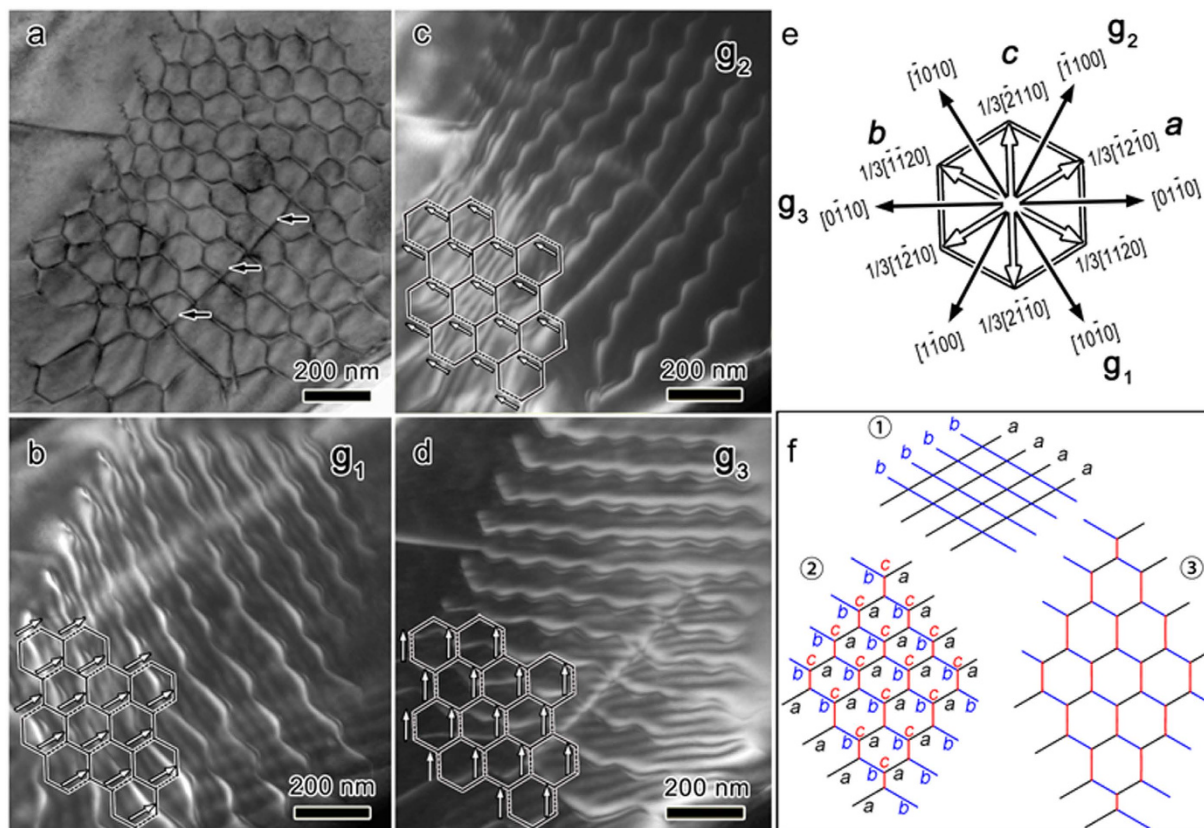


Figure 1. Formation of HSDNs. (a) A typical TEM morphology of HSDNs. Arrows denote unreacted dislocation segments. TEM dark field images are recorded with diffraction vectors (b) g_1 , (c) g_2 and (d) g_3 . Solid and dotted lines illustrate the dislocations in and out of contrast, respectively. White arrows denote the Burgers vectors of the dislocation segments out of contrast. (e) Crystallographic directions of the diffraction vectors and Burgers vectors. (f) Illustrations of the formation of HSDNs. *a*- (black) and *b*-type (blue) dislocation arrays encounter (①), and react to form *c*-type (red) dislocation segments (②). Dislocation configurations evolve to be HSDNs (③). Theoretically, the initial *a*- and *b*-type dislocation arrays can be screw, edge or mixed type. Nevertheless, irrespective of the nature of the initial dislocation arrays, the dislocation segments in the final equilibrium dislocation configuration are screw type. For the sake of simplicity, only the case for screw dislocation arrays is considered.

$g \backslash b$	$1/3[\bar{1}2\bar{1}0]$	$1/3[\bar{1}\bar{1}20]$	$1/3[\bar{2}110]$
$10\bar{1}0$	0	-1	-1
$0\bar{1}10$	-1	1	0
$\bar{1}100$	1	0	1

Table 1. Values of $g \cdot b$ for basal dislocations in Ti_3AlC_2 . Since no stacking faults were observed in the present studies, only the Burgers vectors (b) of full dislocations are considered. Imaged with a diffraction vector g , dislocations with $g \cdot b = 0$ are out of contrast.

morphology. According to the $g \cdot b$ values in Table 1, the Burgers vectors of the dislocation segments out of contrast in Fig. 1b–d are $1/3[\bar{1}2\bar{1}0]$, $1/3[\bar{1}\bar{1}20]$ and $1/3[\bar{2}110]$ (denoted by *a*, *b* and *c*, Fig. 1e), respectively. For the sake of clarity, the dislocation segments in contrast are illustrated by solid lines and those out of contrast are marked with black dotted lines, as shown in Fig. 1b–d. White arrows represent the Burgers vectors of the dislocations out of contrast. Evidently, the Burgers vectors are parallel to the dislocation segments, indicating that the segments are screw type. The dislocation reaction at the nodes is $a + b \rightarrow c$. Figure 1f schematically illustrates the formation of HSDNs. The *a*- and *b*-type dislocation arrays encounter each other and react to form *c*-type segments. Under interaction forces, the final equilibrium configuration of HSDNs is established¹⁶. Theoretically, the initial *a*- and *b*-type dislocation arrays can be screw, edge or mixed type¹⁶, provided equation (1) is satisfied:

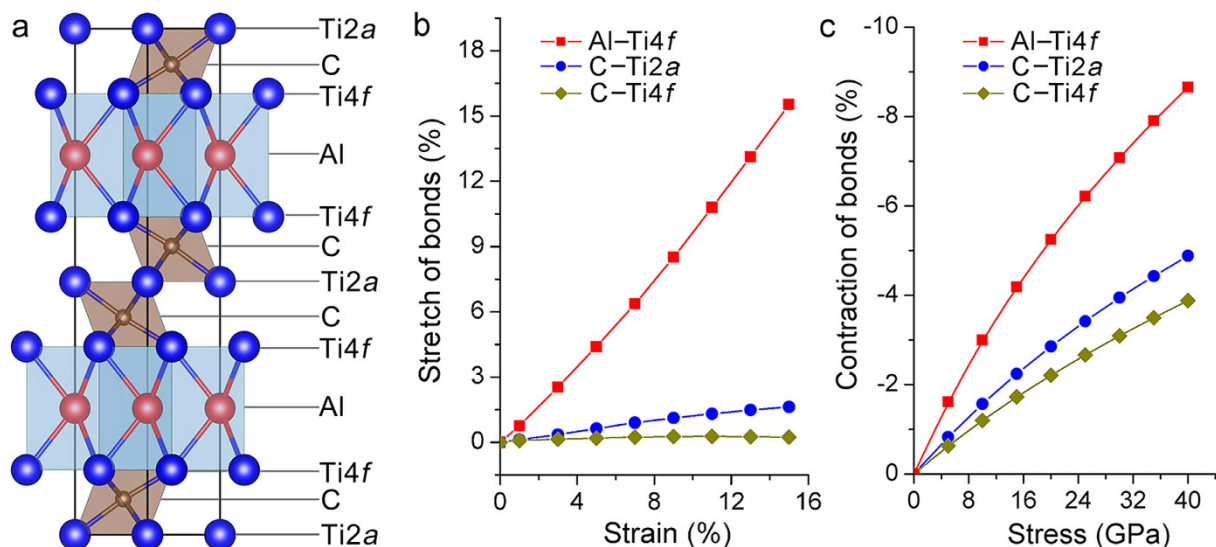


Figure 2. Changes in bond length. (a) Illustration of the unit cell of Ti_3AlC_2 . Ti2a and Ti4f denote the Ti atoms located at the 2a and 4f Wyckoff sites of $P6_3/mmc$, respectively. Changes in bond length of Al-Ti4f, C-Ti2a and C-Ti4f under (b) uniaxial tension along [0001], and (c) hydrostatic compression.

$$\sum_i \mathbf{b}_i^2 \xi_i = 0 \quad (1)$$

where \mathbf{b}_i is the Burgers vector and ξ_i is the direction vector of dislocation line.

Since $a^2 + b^2 > c^2$, the above-mentioned reaction is energetically favorable. However, not all the crossing a - and b -type segments can react to form c -type segments. As marked by the black arrows in Fig. 1a, a long a -type segment fails to react with b -type segments although they intersect at several positions, wherein the intersection angles are approximately 90° . This is more apparent in Supplementary Fig. S1. According to Hirth *et al.*, crossing dislocations that are a few degrees from being orthogonal cannot react¹⁶. Therefore, orthogons (Supplementary Fig. S1) or pentagons (Fig. 1a) instead of hexagons can be identified because of unfavorable dislocation line directions. It is worth noting that, apart from $a + b \rightarrow c$ (marked by the black circle in Supplementary Fig. S1), the reaction $a + c \rightarrow b$ (marked by the red circle in Supplementary Fig. S1) contributes to the formation of HSDNs as well.

The plane of twist sub-grain boundaries. With the formation of HSDNs, SATGBs are established on the basal plane where the networks are located. Then, a scientific question naturally arises: which basal atomic plane is the most likely boundary plane? We address this issue via studies on atomic-scale deformation (illustrations are presented in Supplementary Fig. S2) and general stacking fault energy (GSFE) landscapes. The crystal structure of Ti_3AlC_2 comprises edge-sharing Ti_6C octahedron layers bonded by C-Ti2a and C-Ti4f, and Ti_6Al triangular prism layers bonded by Al-Ti4f (Fig. 2a, Ti2a and Ti4f denote the Ti atoms located at the 2a and 4f Wyckoff sites of $P6_3/mmc$, respectively). Figure 2b plots the changes in bond length for Al-Ti4f, C-Ti2a and C-Ti4f against applied tensile strains along [0001]. It can be seen that the changes in C-Ti2a and C-Ti4f are negligible, and most of the strains are accommodated by the elongation of Al-Ti4f. Specifically, the stretches of Al-Ti4f are 6~10 and 9~66 times those of C-Ti2a and C-Ti4f, respectively. Similar features can be identified in the hydrostatic compression (Fig. 2c), where the contractions of Al-Ti4f are 2~3 times those of C-Ti2a and C-Ti4f. Therefore, Al-Ti4f is the weakest bond in Ti_3AlC_2 , and shear is believed to occur most easily therein.

To further quantitatively confirm this from an energetic point view, GSFE was calculated (see the Methods and Supplementary Fig. S3 for details). The GSFE of Al-Ti4f is significantly lower than those of C-Ti4f and C-Ti2a (Fig. 3a), and the local maximum (USF) of Al-Ti4f is only 18.9% and 12.5% of those of C-Ti2a and C-Ti4f, respectively (Table 2). Besides, the ideal shear strength (maximum restoring force, defined as the maximum slope of the GSFE curve) of Al-Ti4f is only 19.2% and 12.2% of those of C-Ti2a and C-Ti4f, respectively (Table 2), which is consistent with the trend of interplanar spacing. Thereby, the screw dislocations are believed to be initiated by breaking the Al-Ti4f bonds²¹. Further, the SATGBs are most probably located between the Al and Ti4f atomic layers.

Discussion

MAX phases are well recognized to be of bonding anisotropy^{3,22–25}. M_6X octahedron layers are strongly covalently bonded, while adjacent M-X slabs are relatively weakly coupled by M-A metallic bonds. For Ti_3AlC_2 , the ideal shear strength with breaking Al-Ti4f is only 19.2% and 12.2% of those with breaking C-Ti2a and C-Ti4f, respectively (Table 2), indicating that the most probable shear plane is the one between the Al and Ti4f layers²¹. Schematically, the shear of Ti_6Al triangular prisms is illustrated in Fig. 3b. Therefore, the SATGBs observed in

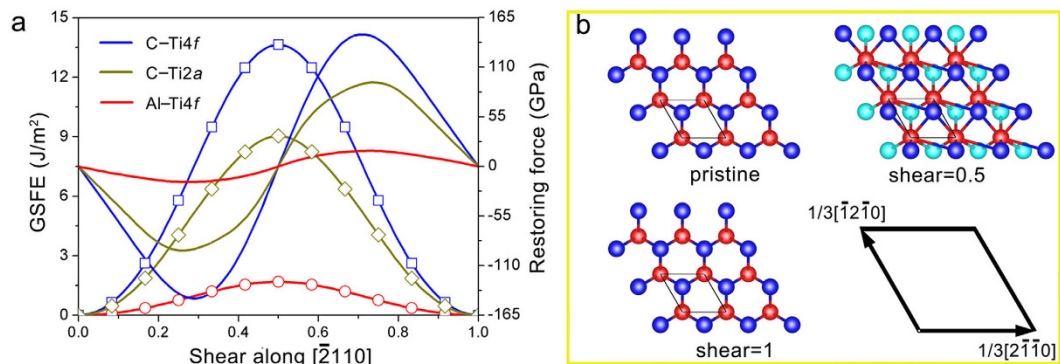


Figure 3. GSFE and restoring force. (a) GSFE (lines with symbols) and restoring force curves for shear deformations with breaking C-Ti4f, C-Ti2a and Al-Ti4f. The shear displacement is normalized by the length of $1/3[\bar{2}110]$. (b) Atomic configurations of Ti_6Al triangular prismatic layers for the shear deformation with breaking Al-Ti4f. Al atoms are denoted by red balls. Balls in cyan and blue highlight the Ti atoms just below and above the slip plane, respectively.

Bonds	USF (J/m ²)	Ideal strength (GPa)	<i>d</i> (Å)
Al-Ti4f	1.7	17.9	2.26
C-Ti2a	9.0	93.4	1.07
C-Ti4f	13.6	146.6	1.31

Table 2. USF, ideal strength and interplanar spacing. USF is the local maximum of the GSFE curve. Ideal strength is defined as the maximum slope of the GSFE curve. *d* is interplanar spacing illustrated in Supplementary Fig. S3.

this study are believed to be there. As a characteristic parameter of the twist boundary, the twist angle, θ , can be estimated by equation (2)^{16,20}:

$$\theta = \frac{b}{\sqrt{3}l_h} \quad (2)$$

where b and l_h are the lengths of the Burgers vector and hexagon edge, respectively. The calculated twist angle in Fig. 1a is approximately 0.26° . Figure 4a–c present the typical TEM morphologies of the HSDNs in the specimens with various deformations (4%, 14% and 26%). As the deformation proceeds, new dislocations intersect and react with the as-formed hexagonal networks. Consequently, small hexagonal dislocation cells form in large cells, and the average cell size diminishes. Statistical data of l_h and θ are plotted in Fig. 4d against the strain. It can be seen that the twist angle scales with the applied strains. For the sample deformed by 26%, the twist angle is about 0.5° . Notably, the HSDNs can be observed in other slowly deformed MAX phases (like Ti_2AlC , Nb_4AlC_3 and *etc.*, Supplementary Fig. S4). The formation of HSDNs/SATGBs is generic to low-energy dislocation configurations in slowly deformed MAX phases. For MAX phases, the collective behavior of basal dislocations includes not only the previously reported accumulation of dislocations vertical and parallel to the basal plane⁹, but also the formation of HSDNs/SATGBs.

Dislocations are the carriers of plastic deformation. Their mutual interactions and reactions bring about work hardening. The formation of HSDNs contributes to previously identified strain hardening of Ti_3AlC_2 ¹¹, giving rise to SATGBs. Since the twist angle is very small (around 0.5°), the contribution of SATGBs to the plastic deformation of Ti_3AlC_2 is quite limited. Sub-grains have been reported in the tensile and compressive creep of MAX phases^{26–28}. Since the SATGBs are formed in compression with remarkably low strain rates, it is inferred that they likely contribute to the creep at high temperature.

With the formation of low energy dislocation structures, misorientations at grain and sub-grain scale are established. The misorientation angle increases with the strain in metals, linearly^{29,30} or in a power law (with an exponent of $1/2$)^{31,32}. Our work indicates that the twist angle scales with the deformation in a roughly linear manner in the investigated strain and temperature ranges.

In summary, small angle twist sub-grain boundaries (around 0.5°) have been ubiquitously observed in uniaxially compressed Ti_3AlC_2 . The twist sub-grain boundaries predominantly comprise hexagonal screw dislocation networks that result from basal dislocation reactions. The grain boundary plane is believed to be between the relatively weakly bonded Al and Ti4f layers. In addition, it is unambiguously demonstrated that the twist angle scales with the deformation. This work may shed light on the formation of low-energy dislocation configurations and its evolution with the deformation of MAX phases.

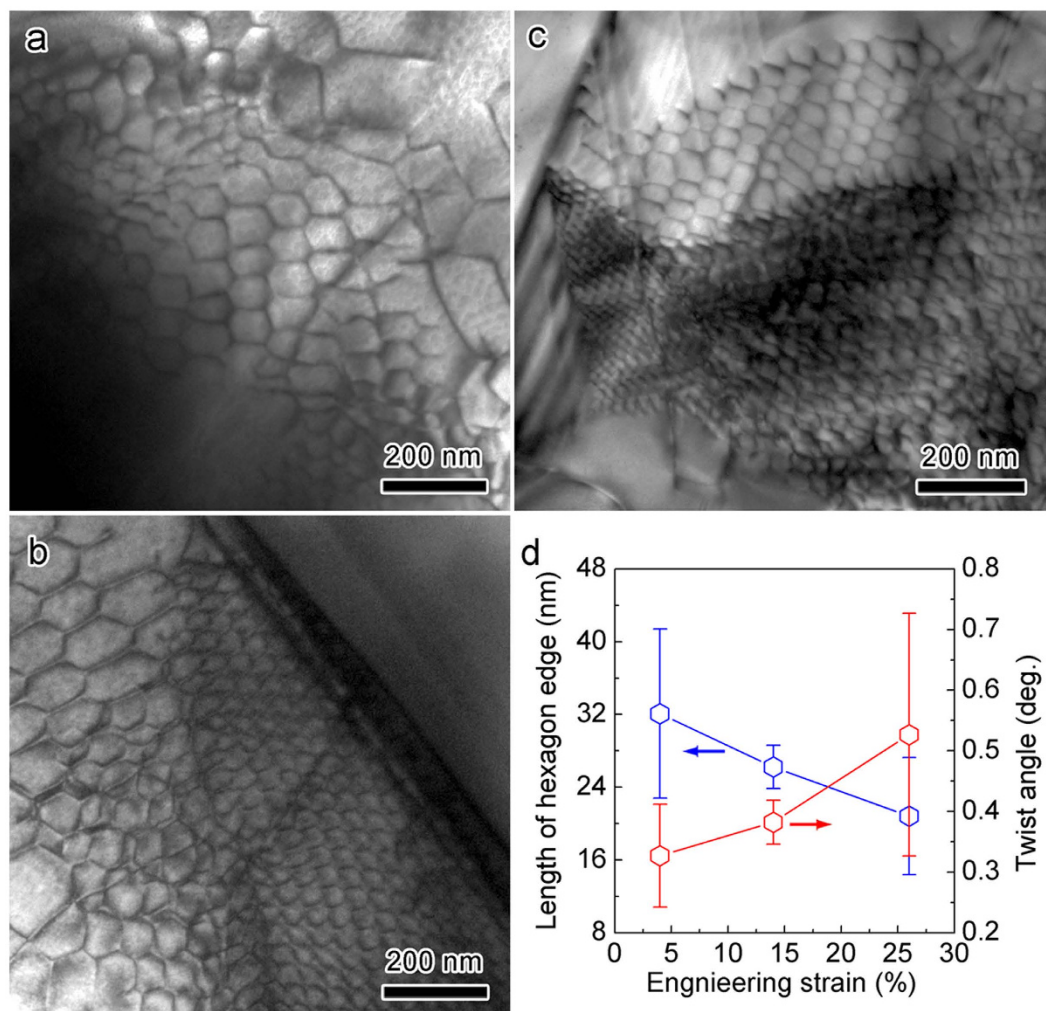


Figure 4. Evolution of twist angle with the deformation. Typical TEM morphologies of HSDNs in the sample deformed by (a) 4%, (b) 14% and (c) 26%. (d) Strain dependence of the length of hexagon edge and twist angle. For the sample with large deformations (14% or 26%), small HSDNs can be identified in the large networks.

Methods

High-temperature deformation. Ti_3AlC_2 bulk sample was synthesized using the method reported by Wang and Zhou³³. For the compression tests, cylinders about 9 mm in diameter and 12 mm in height were cut from the as-prepared sample by electric discharge machining and then mechanically polished. Subsequently, three cylinders were compressed to a strain of 4%, 14% and 26% at 1200 °C with a strain rate of 10^{-5} s^{-1} in a universal testing machine (SANS CMT4204, Shenzhen, China).

TEM characterization. Dislocation configurations were analyzed using a transmission electron microscope (FEI Tecnai G2 F20, Oregon, USA) working at 200 kV. For TEM investigations, slices were cut from the deformed sample in two directions, vertical and parallel to the load. Then, the slices were mechanically thinned and ion-milled to be electron transparent. The Burgers vectors of the dislocations were determined by the **g·b** method. For each deformation, statistics of hexagonal cell size were determined on seven TEM images obtained from different regions.

First-principles calculations. The deformation at atomic scale was modelled with the CASTEP module³⁴. Electronic exchange-correlation energy was treated under a generalized gradient approximation (GGA-PBE)^{35,36}. Interactions of electrons with ion cores were represented by Vanderbilt-type ultrasoft pseudopotential³⁷. The Broyden-Fletcher-Goldfarb-Shanno minimization method was used for geometry optimization, where the plane-wave cut-off energy and the Brillouin zone sampling were fixed at 450 eV and $5 \times 5 \times 2$ Monkhorst-Pack-point meshes³⁸, respectively. Differences in total energy, maximum ionic Hellmann-Feynman force, maximum ionic displacement and maximum stress were converged to $5 \times 10^{-6} \text{ eV/atom}$, 0.01 eV/Å, $5 \times 10^{-4} \text{ Å}$ and 0.02 GPa, respectively. The fully optimized structure was used for uniaxial tension and hydrostatic compression. The deformation modes are illustrated in Supplementary Fig. S2. To ensure a uniaxial deformation along [0001], the lattice parameters perpendicular to the applied strain, as well as the internal coordinates of atoms, were fully relaxed until the stresses were converged to 0.02 GPa. For the GSFE calculation, a supercell with twenty-five

atomic layers with Al layers at the center and surfaces was constructed using the fully optimized Ti_3AlC_2 unit cell, where a vacuum slab of 15 Å in thickness was symmetrically added (see Supplementary Fig. S3). The disregistry on the plane of interest was introduced by rigidly shifting all the atoms above the target plane relative to those below that plane along $\langle\bar{2}110\rangle$. Without relaxing the supercell further, total energies of faulted structures were calculated. Then, the energy difference between the faulted and unfaulted structures gives the GSFE.

References

- Barsoum, M. W. The $\text{M}_{N+1}\text{AX}_N$ phases: a new class of solids; thermodynamically stable nanolaminates. *Prog. Solid State Chem.* **28**, 201–281 (2000).
- Wang, X. H. & Zhou, Y. C. Layered machinable and electrically conductive Ti_2AlC and Ti_3AlC_2 ceramics: a review. *J. Mater. Sci. Technol.* **26**, 385–416 (2010).
- Wang, J. Y. & Zhou, Y. C. Recent progress in theoretical prediction, preparation, and characterization of layered ternary transition-metal carbides. *Annu. Rev. Mater. Res.* **39**, 415–443 (2009).
- Sun, Z. M. Progress in research and development on MAX phases: a family of layered ternary compounds. *Int. Mater. Rev.* **56**, 143–166 (2011).
- Radovic, M. & Barsoum, M. W. MAX phases: bridging the gap between metals and ceramics. *Am. Ceram. Soc. Bull.* **92**, 20–27 (2013).
- Eklund, P., Beckers, M., Jansson, U., Höglberg, H. & Hultman, L. The $\text{M}_{n+1}\text{AX}_n$ phases: materials science and thin-film processing. *Thin Solid Films* **518**, 1851–1878 (2010).
- Barsoum, M. W. & Radovic, M. Elastic and mechanical properties of the MAX Phases. *Annu. Rev. Mater. Res.* **41**, 195–227 (2011).
- Farber, L., Levin, I. & Barsoum, M. W. High-resolution transmission electron microscopy study of a low-angle boundary in plastically deformed Ti_3SiC_2 . *Philos. Mag. Lett.* **79**, 163–170 (1999).
- Barsoum, M. W., Farber, L. & El-Raghy, T. Dislocations, kink bands and room temperature plasticity of Ti_3SiC_2 . *Metall. Mater. Trans. A* **30**, 1727–1738 (1999).
- Zhen, T., Barsoum, M. W. & Kalidindi, S. R. Effects of temperature, strain rate and grain size on the compressive properties of Ti_3SiC_2 . *Acta Mater.* **53**, 4163–4171 (2005).
- Zhang, H., Wang, X. H., Wan, P., Zhan, X. & Zhou, Y. C. Insights into high-temperature uniaxial compression deformation behavior of Ti_3AlC_2 . *J. Am. Ceram. Soc.* **98**, 3332–3337 (2015).
- Guitton, A., Joulain, A., Thilly, L. & Tromas, C. Dislocation analysis of Ti_2AlN deformed at room temperature under confining pressure. *Philos. Mag.* **92**, 4536–4546 (2012).
- Bei, G. P. *et al.* Pressure-enforced plasticity in MAX phases: from single grain to polycrystal investigation. *Philos. Mag.* **93**, 1784–1801 (2013).
- Tromas, C., Villechaise, P., Gauthier-Brunet, V. & Dubois, S. Slip line analysis around nanoindentation imprints in Ti_3SnC_2 : a new insight into plasticity of MAX-phase materials. *Philos. Mag.* **91**, 1265–1275 (2011).
- Guitton, A., Joulain, A., Thilly, L. & Tromas, C. Evidence of dislocation cross-slip in MAX phase deformed at high temperature. *Sci. Rep.* **4**, 6358 (2014).
- Hirth, J. P. & Lothe, J. *Theory of Dislocations* (Wiley, 1982).
- Hull, D. & Bacon, D. J. *Introduction to Dislocations* (Elsevier, 2011).
- Tochigi, E., Kezuka, Y., Shibata, N., Nakamura, A. & Ikuhara, Y. Structure of screw dislocations in a (0001)/[0001] low-angle twist grain boundary of alumina ($\alpha\text{-Al}_2\text{O}_3$). *Acta Mater.* **60**, 1293–1299 (2012).
- Yang, J. B., Osetsky, Y. N., Stoller, R. E., Nagai, Y. & Hasegawa, M. The effect of twist angle on anisotropic mobility of {110} hexagonal dislocation networks in α -iron. *Scr. Mater.* **66**, 761–764 (2012).
- Dai, S., Xiang, Y. & Srolovitz, D. J. Structure and energy of (111) low-angle twist boundaries in Al, Cu and Ni. *Acta Mater.* **61**, 1327–1337 (2013).
- Gouriet, K. *et al.* Dislocation modelling in Ti_2AlN MAX phase based on the Peierls–Nabarro model. *Philos. Mag.* **95**, 2539–2552 (2015).
- Barsoum, M. W. *MAX Phases: Properties of Machinable Ternary Carbides and Nitrides* (Wiley, 2013).
- Guo, Z. L., Zhu, L. G., Zhou, J. & Sun, Z. M. Microscopic origin of MXenes derived from layered MAX phases. *RSC Adv.* **5**, 25403–25408 (2015).
- Du, Y. L., Sun, Z. M., Hashimoto, H. & Tian, W. B. Bonding properties and bulk modulus of M_4AlC_3 ($M = \text{V}, \text{Nb}, \text{and Ta}$) studied by first-principles calculations. *Phys. Status Solidi B* **246**, 1039–1043 (2009).
- He, X. *et al.* General trends in the structural, electronic and elastic properties of the M_3AlC_2 phases ($M =$ transition metal): a first-principle study. *Comput. Mater. Sci.* **49**, 691–698 (2010).
- Zhen, T. *et al.* Compressive creep of fine and coarse-grained Ti_3SiC_2 in air in the 1100–1300 °C temperature range. *Acta Mater.* **53**, 4963–4973 (2005).
- Tallman, D. J., Naguib, M., Anasori, B. & Barsoum, M. W. Tensile creep of Ti_2AlC in air in the temperature range 1000–1150 °C. *Scr. Mater.* **66**, 805–808 (2012).
- Barcelo, F. *et al.* Electron-backscattered diffraction and transmission electron microscopy study of post-creep Ti_3SiC_2 . *J. Alloys Comp.* **488**, 181–189 (2009).
- Hu, H. E., Zhen, L., Zhang, B. Y., Yang, L. & Chen, J. Z. Microstructure characterization of 7050 aluminum alloy during dynamic recrystallization and dynamic recovery. *Mater. Charact.* **59**, 1185–1189 (2008).
- Hu, H. E., Yang, L., Zhen, L., Shao, W. Z. & Zhang, B. Y. Relationship between boundary misorientation angle and true strain during high temperature deformation of 7050 aluminum alloy. *Trans. Nonferrous Met. Soc. China* **18**, 795–798 (2008).
- Gurao, N. P. & Suwas, S. Generalized scaling of misorientation angle distributions at meso-scale in deformed materials. *Sci. Rep.* **4**, 5641 (2014).
- Hughes, D. A., Chrzan, D. C., Liu, Q. & Hansen, N. Scaling of misorientation angle distributions. *Phys. Rev. Lett.* **81**, 4664 (1998).
- Wang, X. H. & Zhou, Y. C. Solid–liquid reaction synthesis of layered machinable Ti_3AlC_2 ceramic. *J. Mater. Chem.* **12**, 455–460 (2002).
- Segall, M. D. *et al.* First-principles simulation: ideas, illustrations and the CASTEP code. *J. Phys.: Condens. Matter* **14**, 2717–2744 (2002).
- Perdew, J. P., Burke, K. & Ernzerhof, M. Generalized gradient approximation made simple. *Phys. Rev. Lett.* **77**, 3865 (1996).
- Perdew, J. P. *et al.* Atoms, molecules, solids, and surfaces: applications of the generalized gradient approximation for exchange and correlation. *Phys. Rev. B* **46**, 6671 (1992).
- Vanderbilt, D. Soft self-consistent pseudopotentials in a generalized eigenvalue formalism. *Phys. Rev. B* **41**, 7892 (1990).
- Pack, J. D. & Monkhorst, H. J. “Special points for Brillouin-zone integrations” – a reply*. *Phys. Rev. B* **16**, 1748 (1977).

Acknowledgements

This work was supported by the Chinese Academy of Sciences (CAS) and Shenyang National Laboratory for Materials Science, Institute of Metal Research, CAS.

Author Contributions

H.Z. and C.Z. carried out the sample synthesis and microstructure characterization. H.Z. and T.H. conducted the first-principles calculations. X.H.W. conceived and designed the project. H.Z., X.H.W., X.Z. and Y.C.Z. wrote the paper. All authors contributed to data analysis and scientific discussion.

Additional Information

Supplementary information accompanies this paper at <http://www.nature.com/srep>

Competing financial interests: The authors declare no competing financial interests.

How to cite this article: Zhang, H. *et al.* On the small angle twist sub-grain boundaries in Ti_3AlC_2 . *Sci. Rep.* **6**, 23943; doi: 10.1038/srep23943 (2016).



This work is licensed under a Creative Commons Attribution 4.0 International License. The images or other third party material in this article are included in the article's Creative Commons license, unless indicated otherwise in the credit line; if the material is not included under the Creative Commons license, users will need to obtain permission from the license holder to reproduce the material. To view a copy of this license, visit <http://creativecommons.org/licenses/by/4.0/>